Response of El Niño sea surface temperature variability to greenhouse warming

Seon Tae Kim[1]*, Wenju Cai[1,2]*, Fei-Fei Jin[3], Agus Santoso[4], Lixin Wu[2], Eric Guilyardi[5,6] and Soon-Il An[7]

The destructive environmental and socio-economic impacts of the El Niño/Southern Oscillation[1,2] (ENSO) demand an improved understanding of how ENSO will change under future greenhouse warming. Robust projected changes in certain aspects of ENSO have been recently established[3–5]. However, there is as yet no consensus on the change in the magnitude of the associated sea surface temperature (SST) variability[6–8], commonly used to represent ENSO amplitude[1,6], despite its strong effects on marine ecosystems and rainfall worldwide[1–4,9]. Here we show that the response of ENSO SST amplitude is time-varying, with an increasing trend in ENSO amplitude before 2040, followed by a decreasing trend thereafter. We attribute the previous lack of consensus to an expectation that the trend in ENSO amplitude over the entire twenty-first century is unidirectional, and to unrealistic model dynamics of tropical Pacific SST variability. We examine these complex processes across 22 models in the Coupled Model Intercomparison Project phase 5 (CMIP5) database[10], forced under historical and greenhouse warming conditions. The nine most realistic models identified show a strong consensus on the time-varying response and reveal that the non-unidirectional behaviour is linked to a longitudinal difference in the surface warming rate across the Indo-Pacific basin. Our results carry important implications for climate projections and climate adaptation pathways.

ENSO events are characterized by anomalous warming and cooling in the eastern equatorial Pacific, whose intensity is conventionally measured by the Niño3.4 index, an area average of SST anomalies over 5° N–5° S and 170° W–120° W. The Niño3.4 index is positive during El Niño and negative during La Niña. As demonstrated by the standard deviation of the Niño3.4 index over 20-, 30- 40-, or 50-year running periods starting in 1950 (Fig. 1a,b), available observations[11,12] consistently show that the amplitude of ENSO SST variability has enhanced over the past several decades, although a slightly negative trend has commenced in the late 1990s. The statistics show that 1980–2000 was a period of particularly intense ENSO activities, signified by the two most extreme El Niño events in 1982 and 1997 (refs 1,2). The exceptionally warm eastern equatorial Pacific Ocean during these El Niño events caused massive disruption to the marine ecosystem off Peru when the trade winds severely weakened, deepening the thermocline, and cutting off the supply of upwelled nutrients[9]. Other destructive effects include, but are not limited to, coral bleaching and severe alteration of global rainfall patterns[1–4,9]. It is thus of broad

interest to determine how ENSO SST amplitude will respond to greenhouse warming.

Although recent studies have uncovered robust projected changes in ENSO-driven rainfall variability[3,4] and ENSO propagation characteristics[5], there is still no consensus on the change in ENSO SST variability[6–8]. Here we examine the issue using 22 CMIP5 coupled general circulation models (CGCMs) forced under the historical and greenhouse warming (representative concentration pathway 8.5; RCP8.5) conditions (Methods). We show that a consensus emerges by considering both the possibility of the time-dependent response of ENSO amplitude to increased greenhouse gases, which was suggested by a theoretical study[13], and the complex dynamical processes that give rise to the SST anomalies. These two factors in conjunction have not been considered by previous studies[6–8] using CMIP models.

Theoretical, modelling and observational studies indicate that ENSO amplitude is strongly linked to the slowly evolving mean tropical Pacific trade winds, which drive the mean equatorial Pacific thermocline depth[6,14–17]. Concurrent with the observed ENSO amplitude increase, the observed central-to-western equatorial Pacific easterlies[18,19] slackened before the late 1990s, and the slightly weakening trend since then has been associated with the strengthening of the mean easterlies (Fig. 1c), consistent with recent studies[16,20]. Thus, the linkage to the mean easterly winds is an important element of the observed time-varying ENSO amplitude.

The generation of ENSO SST anomalies involves a suite of positive air–sea feedback processes that constitute the Bjerknes feedback[21], operating against various negative feedback processes. The Bjerknes feedback depicts a series of processes in which anomalous equatorial westerly winds cause weakened upwelling, flattened thermocline slope, and sea surface warming that in turn reinforces the wind anomalies. Although nonlinear aspects of ENSO are recognized[22], the overall ENSO dynamics are approximately linear[14,21], as described by the widely used Bjerknes coupled stability (BJ) index[17,23] formula (Supplementary Methods). The BJ index formula partitions the various feedback processes into three positive (zonal advective, thermocline, and Ekman feedbacks) and two negative (mean advection damping and thermodynamic damping) terms.

The performance of CGCMs in simulating these feedback processes and their relative importance varies vastly[24]. As evidenced in our analysis below, this contributes to large uncertainty in the projected change in ENSO amplitude. We compare the BJ index terms from each model with those from observations over the

---

[1]CSIRO Marine and Atmospheric Research, Aspendale, Victoria 3195, Australia, [2]Physical Oceanography Laboratory, Qingdao Collaborative Innovation Center of Marine Science and Technology, Ocean University of China, Qingdao 266003, China, [3]Department of Meteorology, University of Hawaii at Manoa, Honolulu, Hawaii 96822, USA, [4]ARC Centre of Excellence for Climate System Science and Climate Change Research Centre, University of New South Wales, Sydney 2052, Australia, [5]LOCEAN, IPSL, 75252 Paris Cedex 05, France, [6]NCAS-Climate, University of Reading, Reading RG6 6BB, UK, [7]Department of Atmospheric Sciences, Yonsei University, Seoul 120-749, Korea. *e-mail: seontae.kim@csiro.au; wenju.cai@csiro.au
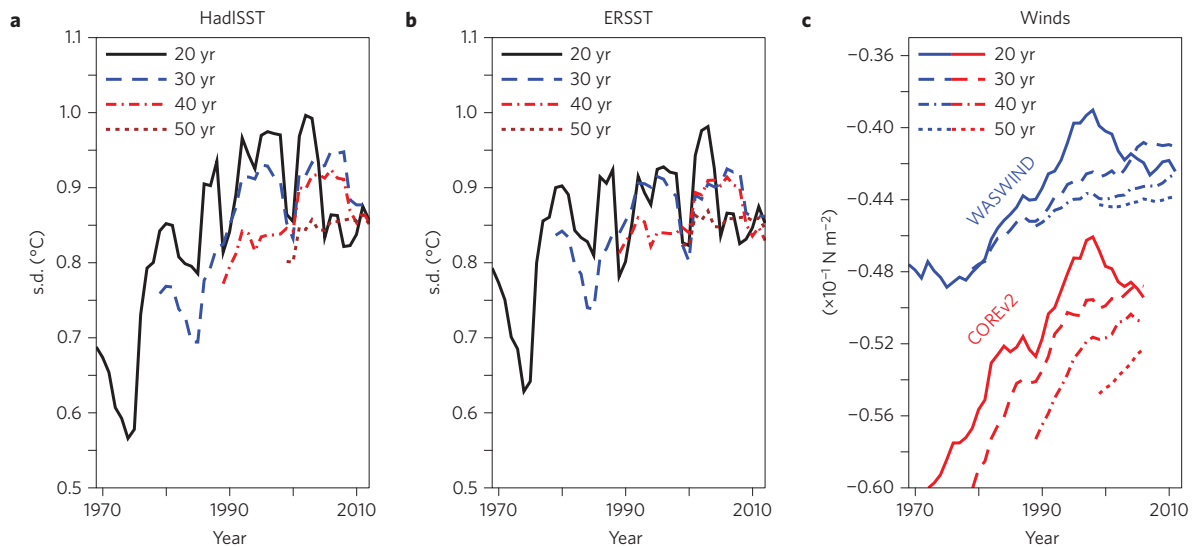
Figure 1 | Observed ENSO amplitude and topical Pacific zonal winds. a,b, ENSO amplitude (°C), defined as the standard deviation of the Niño3.4 index over 20-, 30-, 40- and 50-year windows moving forward starting at every year from 1950 to 2012, using the HadISST (ref. 11; **a**) and ERSST (ref. 12; **b**) data sets. **c**, Climatological zonal wind stress (10^{-1} N m^{-2}) averaged in the central-to-western tropical Pacific (10° S–10° N, 156° E–144° W) over 20-, 30-, 40-, and 50-year running periods from the WASWind[18] over 1950–2009 and the CORE (ref. 19) version 2 over 1950–2006. In **a–c**, the last year of each running period is plotted on the *x* axis.
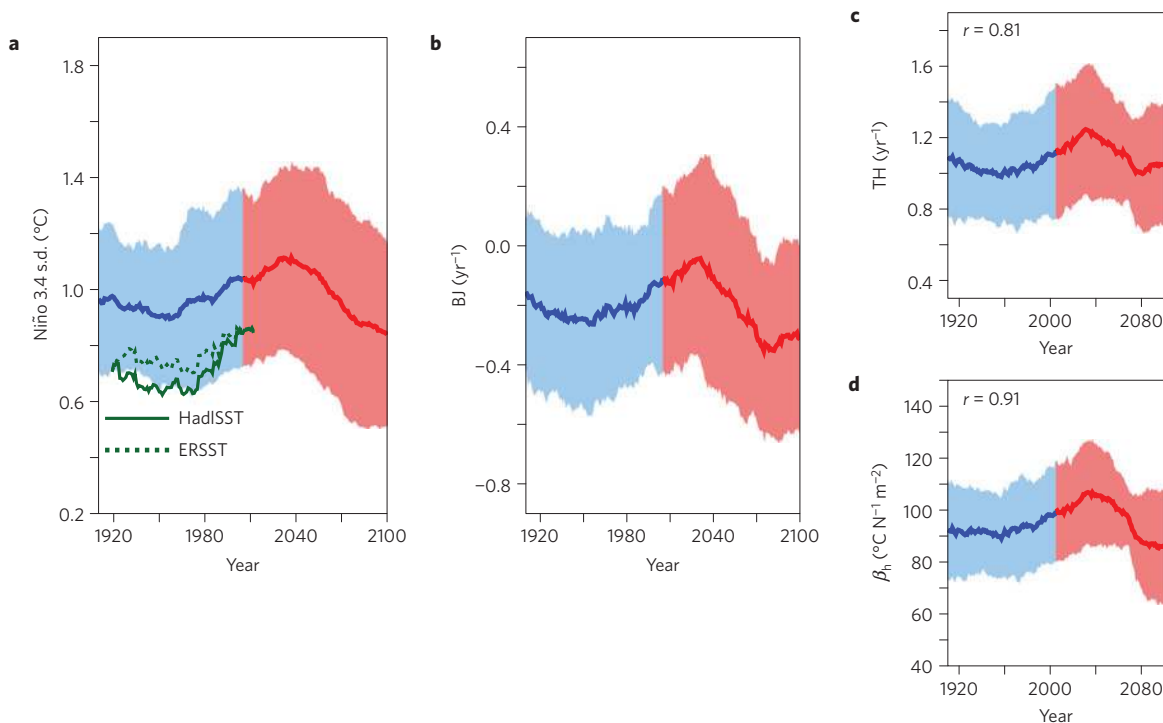

Figure 2 | Time variation of simulated ENSO amplitude and ENSO stability. a, The MME of the ENSO amplitude from the BEST9 computed over 50-year running periods from 1861 to 2100. The 50-year running ENSO amplitudes from HadISST (ref. 11) and ERSST (ref. 12) over the period 1870–2012 are also shown. There is significant correlation between the MME and observations ($r = 0.90$ for HadISST and $r = 0.87$ for ERSST). **b–d**, The MME of the 50-year running ENSO stability estimated using the BJ index (**b**), the MME thermocline feedback term (**c**), and MME response sensitivity coefficient for anomalous zonal thermocline slope response to wind stress anomalies (β_h; **d**) from the BEST9. In **c**, correlation coefficient with the BJ index, and in **d**, correlation coefficient with the thermocline feedback are shown. In **a–d**, light blue shading and light red shading represent inter-model spread or uncertainty range, which is estimated with the inter-model standard deviations, in the historical run and the RCP8.5 run, respectively. The last year of each 50-year running period is plotted on the *x* axis.

latter half of the twentieth century (Supplementary Fig. 1 and Methods). Nine CMIP5 CGCMs (BEST9) are found to be the best in reproducing the relative magnitudes of the observed BJ index

and its five contributing feedback terms. The multi-model ensemble (MME) of the BEST9 is evaluated, and then compared with the MME of the remaining 13 less realistic models (REM13).

The standard deviations of the Niño3.4 index, the BJ index and its contributing terms over 50-year running periods from 1861 to 2100 exhibit a time-varying behaviour (Fig. 2 and Supplementary Fig. 2). The length of the running period of 50 years is chosen to capture a sufficient number of ENSO events, and our results are not sensitive to different lengths of the running period (Supplementary Fig. 3). The aggregated BEST9 shows both an increasing trend of ENSO amplitude over the recent decades and a slightly weakening trend during the early twenty-first century as in the observations (Fig. 2a and Supplementary Fig. 3c).

The increase in ENSO amplitude in BEST9 resumes after 2010 and continues until approximately 2040, reaching an aggregated magnitude ($1.12\,^\circ\text{C} \pm 0.33$) about 13% greater than the post-1950 average ($0.99\,^\circ\text{C}$). After 2040, the ENSO amplitude trend commences a reversal. By the end of the twenty-first century, the ENSO amplitude ($0.84\,^\circ\text{C} \pm 0.32$) decreases to approximately 5% lower than the post-1950 strength. The ENSO evolution in BEST9 is supported by a strong inter-model consensus (Supplementary Table 1). Without considering this time-variation aspect, that is, by simply taking the average difference in ENSO amplitude between the twentieth and twenty-first centuries, as done in previous studies[6–8], robustness on projected change in ENSO amplitude is weakened (Supplementary Table 2).

The evolution of the BJ index shares similar time-varying behaviour to the modelled ENSO amplitude (Fig. 2b), with a high positive correlation ($r = 0.9$), confirming that the BJ index captures the overall dynamics of ENSO. The enhanced ENSO amplitude before 2040 is accompanied by an increasing BJ index, implying that the climate system is changing towards a less damped state, and vice versa with a reduced ENSO amplitude and BJ index thereafter.

As the ENSO feedbacks might vary under greenhouse warming, affecting ENSO amplitude[14], we examine the evolution of all feedback terms. We find that the time-varying BJ index and thus ENSO amplitude are predominantly controlled by evolution of the thermocline feedback, the most dominant positive feedback term[17,20,23,25]. This is evidenced by a correlation coefficient (0.81) of the BJ index with the thermocline feedback component (Fig. 2c), higher than the correlation with any other contributing terms (Supplementary Fig. 2a–d).

The strength of the thermocline feedback is most closely associated with the response of the zonal thermocline slope to a wind anomaly[24] (β_h) among its contributing factors (Supplementary Methods), which is also true for the time evolution of the thermocline feedback because the feedback has the highest correlation (0.91) with β_h (Fig. 2d and Supplementary Fig. 2e–g). Thus, to investigate the associated mechanism, we examine what controls the time variation in β_h.

The strength of β_h varies with the climatological zonal thermocline slope, increasing as the thermocline slope flattens over the 1950–2040 period, but decreasing thereafter as the thermocline slope steepens (Fig. 3a). The climatological zonal thermocline slope, in turn, varies with changes in central-to-western equatorial Pacific mean trade winds (Fig. 3b), influencing ENSO amplitude through the thermocline feedback. We note that over the 1950–2100 period, the reversal in ENSO amplitude trend is marked by a switch from a weakened easterly wind before approximately 2040 to an enhanced easterly thereafter.

The time-varying mean wind is in turn related to the change in the zonal climatological SST gradient induced by different warming rates across the Indo-Pacific Ocean (Fig. 3c). For the period 2010–2040, a greater acceleration in warming occurs in the eastern Pacific than in the eastern Indian–western Pacific (Fig. 4a,b), weakening easterlies over the central-to-western tropical Pacific (Fig. 4c). For the period between 2040 and 2100, the eastern Pacific warming rate abates but a faster warming emerges over the eastern Indian–western Pacific region (Fig. 4b). This differing warming rate
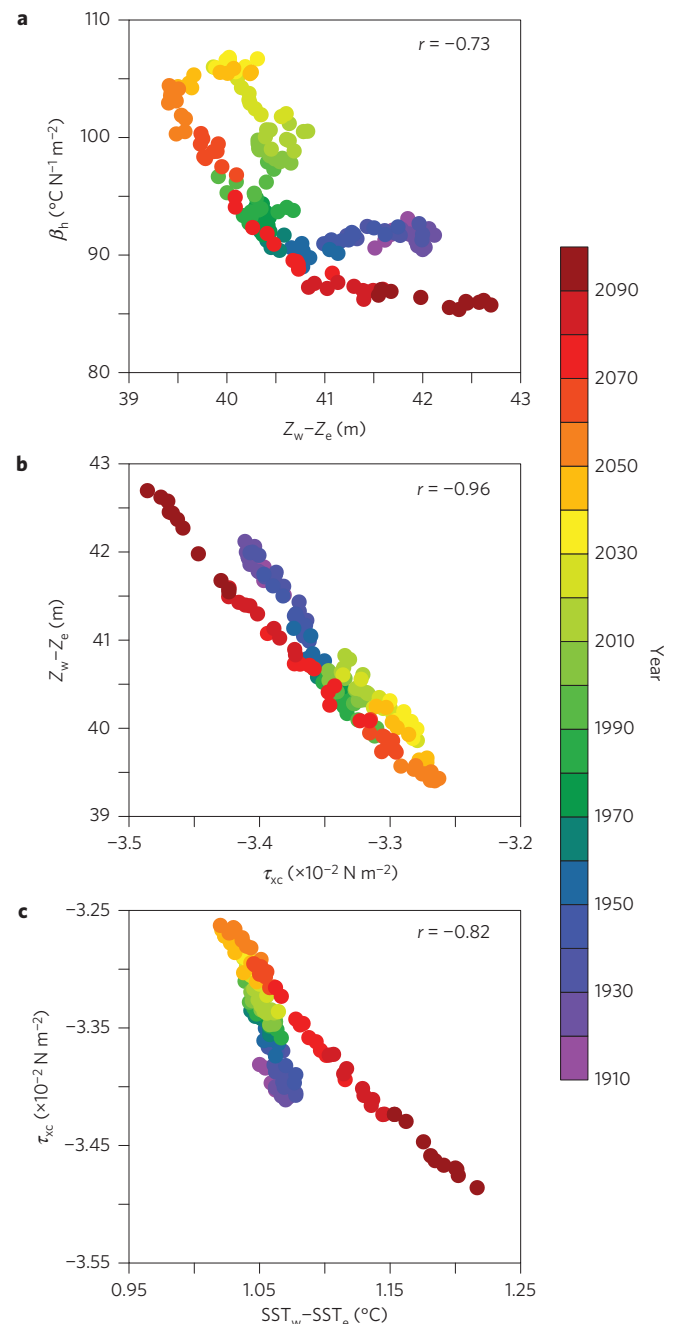

Figure 3 | Factors driving a coupling intensity between anomalous thermocline slope and surface wind in the equatorial Pacific. a, Scatter plots of the MME response sensitivity coefficient (β_h) for zonal thermocline slope response to surface wind stress anomalies versus the MME of climatological zonal thermocline slope in the equatorial Pacific ($Z_w - Z_e$), computed from the BEST9 over 50-year running periods from 1861 to 2100 (Methods). **b,c**, Scatter plots of MME climatological central-to-western Pacific surface wind stress (τ_{xc}) versus MME climatological zonal thermocline slope in the equatorial Pacific (**b**), and versus MME climatological zonal gradient of SST between the eastern Indian–western Pacific and the eastern Pacific (SST$_w$–SST$_e$; **c**). In **a–c**, coloured circles represent the last year of each 50-year running period.

enhances the Indo-Pacific west-minus-east SST gradient and thus enhances the easterlies (Fig. 4c).

One of the mechanisms for the differential warming rate is associated with an eastward migration of higher positive sea level
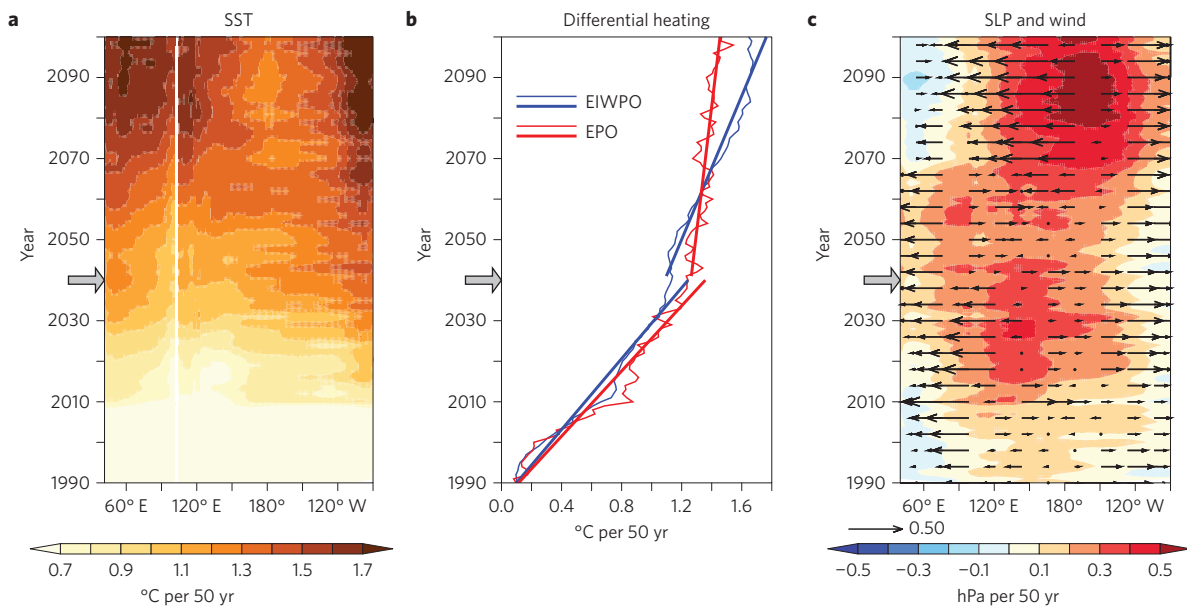
Figure 4 | Time-varying MME linear trends. a, Hovmoller diagram of MME linear trends of SST (°C per 50 yr) across the Indo-Pacific Ocean averaged between 5° S and 5° N over the period 1990–2100. **b**, MME linear trends of SST area-averaged (Methods) over the eastern Pacific (EPO) and over the eastern Indian–western Pacific (EIWPO), with a linear fitting line showing the difference in acceleration of warming across the Indo-Pacific Ocean over the two time periods. The regression line is obtained separately in 1990–2040 and 2041–2100. **c**, The same as in **a** but for MME linear trends of SLP (colour scale) and zonal wind stresses (vectors; 10^{-2} N m^{-2} per 50 yr). In **a–c**, the last year of each 50-year running period is plotted on the *y* axis. The marked grey arrow on the left side of the *y* axis indicates the year 2040, when the ENSO amplitude is projected to begin its reversal.

pressure (SLP) trends over the western Pacific region (Fig. 4c and Supplementary Fig. 4a). This bears some resemblance to the observed interannual atmosphere anticyclone–SST pattern following a mature El Niño phase[26]. During the early period of greenhouse warming (that is, pre-2040), a faster warming in the eastern tropical Pacific (Fig. 4a,b; also ref. 27) is associated with a more elevated SLP over the western Pacific than over the eastern Pacific (Fig. 4c). A stronger warming rate in the eastern equatorial than the eastern subtropical Pacific (Supplementary Figs 4c and 5a; also ref. 28) leads to strengthened northeasterly winds. To the east of the western Pacific high positive SLP trend region, the enhanced total wind speeds increase evaporative cooling, which limits the warming of local SSTs (Supplementary Fig. 4b), and thus result in an eastward progression of relatively weak warming and high positive SLP trends (Supplementary Figs 4a and 5a). The enhanced easterly winds to the south of the progressed SLP trend region also strengthen oceanic upwelling in the central-to-eastern equatorial Pacific, limiting the westward expansion of the eastern Pacific warming (Supplementary Fig. 5a). After 2040, these processes (see schematic picture in Supplementary Fig. 6) lead to an increase in the Indo-Pacific zonal west-minus-east SST gradient, which further intensifies the mean central-to-western equatorial Pacific easterlies (Figs 3c and 4c).

This mechanism is not effective in the REM13, which instead seems to exhibit a persistent increase in ENSO amplitude and BJ index (Supplementary Fig. 7) with a weak inter-model consensus on the amplitude trend (Supplementary Table 1). The SST warming rate in the subtropical region is of comparable magnitude to that in the equatorial Pacific region (Supplementary Fig. 5b), in contrast to the BEST9. The different warming pattern in the REM13, instead weakens the meridional SST gradient (Supplementary Fig. 4f) and the northeasterly winds, leading to less efficient evaporative cooling (Supplementary Fig. 4d,e) than in the case of the BEST9. As a result, there is a further expansion of the relatively large equatorial and subtropical warming towards the central Pacific, hence weakening zonal SST gradients across the Indo-Pacific (Supplementary Fig. 5b).

These zonal SST gradients weaken mean central-to-western Pacific easterlies ($r = -0.99$ between the winds and the mean zonal SST gradient), flattening the equatorial Pacific mean thermocline slope ($r = -0.98$ between the winds and the thermocline slope), and leading to a continuous increase in the thermocline feedback and hence ENSO amplitude.

The difference between the time-varying ENSO amplitude projected by the REM13 and the BEST9 could be due to the REM13 suffering from a more severe cold SST bias along the Equator than the BEST9 (Supplementary Fig. 8), consistent with the less realistic ENSO feedbacks[24]. This highlights that model biases can also contribute to a lack of inter-model consensus on projected ENSO amplitude.

Our result of a time-varying response of ENSO SST variability to greenhouse warming during the twenty-first century, with initially increasing ENSO amplitude followed by decreasing amplitude, is in sharp contrast to the previous expectation of a unidirectional change in studies using CMIP models. This non-unidirectional change revealed here suggests an enhanced ENSO SST variability in the Pacific and its extended effects over the next two to three decades.

Methods

Boxed regions. For the BJ index analysis (Supplementary Methods), the western and eastern boxed regions were determined considering the model's own ENSO. They extend from 82° W westward and from 121° E eastward, respectively, to a longitude (H_c; Supplementary Table 3) where the zero contour line passes the Equator in the regressed pattern of oceanic heat content anomalies with the first principal component of the empirical orthogonal function for SST anomalies in the tropical Pacific (120° E–80° W, 20° S–20° N) from individual coupled models and reanalysis data[29]. The latitudinal range of the boxed region is 5° S–5° N. The H_c was also applied to calculations in Fig. 3. The zonal thermocline slope (Fig. 3a,b) is defined as the difference of thermocline depth (the depth of maximum temperature gradient within 0–400 m) between the western equatorial Pacific (121° E–H_c, 5° S–5° N) and the eastern Pacific (H_c – 82° W, 5° S–5° N). The central-to-western tropical Pacific climatological mean wind stresses (Fig. 3b,c) are averaged over H_c –30°-H_c +30° in longitude and 5° S–5° N in latitude. The climatological zonal SST gradient (Fig. 3c) is the difference between the eastern Indian–western tropical Pacific (60° E–120° E, 10° S–10° N) SST and the eastern

Pacific ($H_c - H_c + 60°$, 10° S–10° N) SST. This boxed region is also applied to Fig. 4b.

CMIP5 models. We analysed the historical runs over the period 1861–2005 and RCP8.5 experiments over the period 2006–2100 from 22 CMIP5 models to represent the present-day climate and future warmer climate, respectively; the former runs are forced by observed atmospheric compositions over the twentieth century and the latter runs by a high greenhouse gas emission scenario with a radiative forcing that increases to a level of 8.5 W m^{-2} at the end of the twenty-first century. The models include ACCESS1-0, ACCESS1-3, CCSM4, CNRM-CM5, CSIRO-MK3-6-0, FGOALS-g2, GFDL-CM3, GFDL-ESM2G, GFDL-ESM2M, GISS-E2-R, HadGEM2-CC, HadGEM2-ES, IPSL-CM5A-LR, IPSL-CM5A-MR, IPSL-CM5B-LR, MIROC5, MIROC-ESM, MPI-ESM-LR, MPI-ESM-MR, MRI-CGCM3, NorESM1-M and NorESM1-ME. More detailed information on CMIP5 coupled models can be obtained from http://cmip-pcmdi.llnl.gov/cmip5/availability.html.

MME analysis. For the MME analysis, we selected CMIP5 models that have realistic, relative contributions of the three positive and the two negative feedback terms to ENSO stability, as estimated by the BJ index, in comparison with those from the reanalysis data sets. We compared the BJ index and its contributing feedback terms from each of the 22 CMIP5 models over the period 1950–1999 with those from the reanalysis data sets over the period 1958–1999. The reanalysis data sets include ocean potential temperatures, ocean currents, and wind stresses from the Simple Ocean Data Assimilation Reanalysis version 2.0.2 (ref. 29) available over the 1958–2007 period and net heat fluxes from the 40-year European Centre for Medium-Range Weather Forecasts Reanalysis[30] over the 1958–2001 period. The correlation coefficients and root mean square error (r.m.s.e.) between each model and the reanalysis were calculated in terms of the relative importance of the five BJ index contributing terms and the BJ index, following the sequence shown in Supplementary Fig. 1. Each model and the reanalysis have six samples (five BJ terms and one BJ index), all in an identical sequence, which permits calculation of the correlation coefficients and r.m.s.e. The selected nine models (GFDL-CM3, GFDL-ESM2M, MIROC5, GISS-E2-R, FGOALS-g2, NorESM1-M, NorESM1-ME, CCSM4, ACCESS1-0) have a significant correlation at the 99% confidence level and also a relatively small r.m.s.e. (that is, red-coloured models in Supplementary Fig. 1) among the 22 CMIP5 models. The MME, which is obtained by simply averaging all models of each group without applying a weight to each model, is calculated separately for the BEST9 and the REM13. The utilization of the BJ index for selecting models is addressed in the Supplementary Information.

Statistical analysis. To examine how various quantities (including ENSO amplitude, BJ index, climatology, and linear trends) vary over time, in each model we combined the two experiments to form a 240-year-long data set as the RCP8.5 experiments start from 1 January 2006 of the historical runs, and performed analyses over running periods from 1861 to 2100.

Anomalous quantities are departures from a running climatology. In other words, they are obtained by removing the long-term mean seasonal cycle of each running period. A linear trend is computed by a least-squares fit of the monthly anomalous quantities. Before the BJ index analysis, the linear trend is removed from the anomalies and a seven-year running mean was also applied to remove decadal and longer variation (for example, Supplementary Figs 9–11).

For the observed SST, we use two reanalysis data sets, that is, Hadley Centre sea ice and SST version 1 (HadISST; ref. 11) and extended reconstructed SST (ERSST) version 3b (ref. 12) over the period 1871–2012. To examine the observed central-to-western tropical Pacific mean zonal winds, we use the WASWind[18] (1950–2009) and CORE version 2 (ref. 19) (1950–2006) data sets.

References

1. McPhaden, M. J., Zebiak, S. E. & Glantz, M. H. ENSO as an integrating concept in earth science. *Science* **314,** 1740–1745 (2006).
2. Philander, S. G. H. Anomalous El Niño of 1982–83. *Nature* **305,** 16 (1983).
3. Cai, W. *et al.* Increasing frequency of El Niño events due to greenhouse warming. *Nature Clim. Change* **4,** 111–116 (2014).
4. Power, S., Delage, F., Chung, C., Kociuba, G. & Keay, K. Robust twenty-first-century projections of El Niño and related precipitation variability. *Nature* **502,** 541–545 (2013).
5. Santoso, A. *et al.* Late-twentieth-century emergence of the El Niño propagation asymmetry and future projections. *Nature* **504,** 126–130 (2013).
6. Guilyardi, E. El Niño-mean state-seasonal cycle interactions in a multi-model ensemble. *Clim. Dynam.* **26,** 329–348 (2006).
7. Collins, M. *et al.* The impact of global warming on the tropical Pacific Ocean and El Niño. *Nature Geosci.* **3,** 391–397 (2010).
8. Stevenson, S. L. Significant changes to ENSO strength and impacts in the twenty-first century: Results from CMIP5. *Geophys. Res. Lett.* **39,** L17703 (2012).
9. Chavez, F. P., Ryan, J., Lluch-Cota, S. E. & Ñiquen, M. From anchovies to sardines and back: Multidecadal change in the Pacific Ocean. *Science* **299,** 217–221 (2003).
10. Taylor, K. E., Stouffer, R. J. & Meehl, G. A. An overview of CMIP5 and the experimental design. *Bull. Am. Meteorol. Soc.* **93,** 485–498 (2012).
11. Rayner, N. A. *et al.* Global analyses of sea surface temperature sea ice, and night marine air temperature since then late nineteenth century. *J. Geophys. Res.* **108,** 4407 (2003).
12. Smith, T. M., Reynolds, R. W., Peterson, T. C. & Lawrimore, J. Improvements to NOAA's historical merged land-ocean surface temperature analysis (1880–2006). *J. Clim.* **21,** 2283–2296 (2008).
13. Sun, D-Z. El Niño: A coupled response to radiative heating? *Geophys. Res. Lett.* **24,** 2031–2034 (1997).
14. Fedorov, A. V. & Philander, G. Is El Niño changing? *Science* **288,** 1997–2002 (2000).
15. Van Oldenborgh, G. J., Philip, S. Y. & Collins, M. El Niño in a changing climate: A multi-model study. *Ocean Sci.* **1,** 81–95 (2005).
16. McPhaden, M. J., Lee, T. & McClurg, D. El Niño and its relationship to changing background conditions in the tropical Pacific Ocean. *Geophys. Res. Lett.* **38,** L15709 (2011).
17. Kim, S. T. & Jin, F-F. An ENSO stability analysis. Part I: Results from a hybrid coupled model. *Clim. Dynam.* **36,** 1593–1607 (2011).
18. Tokinaga, H. & Xie, S-P. Wave- and Anemometer-based sea surface wind (WASWind) for climate change analysis. *J. Clim.* **24,** 267–285 (2011).
19. Large, W. G. & Yeager, S. G. The global climatology of an interannually varying air–sea flux data set. *Clim. Dynam.* **33,** 341–364 (2009).
20. Luebbecke, J. & McPhaden, M. J. Assessing the 21st century shift in ENSO variability in terms of the Bjerknes stability index. *J. Clim.* **27,** 2577–2587 (2014).
21. Jin, F-F. An equatorial ocean recharge paradigm for ENSO. Part I: Conceptual model. *J. Atmos. Sci.* **54,** 811–829 (1997).
22. An, S-I. & Jin, F-F. Nonlinearity and asymmetry of ENSO. *J. Clim.* **17,** 2399–2412 (2004).
23. Jin, F-F., Kim, S. T. & Bejarano, L. A coupled-stability index of ENSO. *Geophys. Res. Lett.* **33,** L23708 (2006).
24. Kim, S. T., Cai, W., Jin, F-F. & Yu, J-Y. ENSO stability in coupled climate models and its association with mean state. *Clim. Dynam.* **42,** 3313–3321 (2013).
25. Ren, H. & Jin, F-F. Recharge oscillator mechanisms in two types of ENSO. *J. Clim.* **26,** 6506–6523 (2013).
26. Wang, B., Wu, R. & Fu, X. Pacific-East Asian teleconnection: How does ENSO affect East Asian climate? *J. Clim.* **13,** 1517–1536 (2000).
27. Vecchi, G. & Soden, B. Global warming and the weakening of the tropical circulation. *J. Clim.* **20,** 4316–4340 (2007).
28. Xie, S-P. *et al.* Global warming pattern formation: Sea surface temperature and rainfall. *J. Clim.* **23,** 966–986 (2010).
29. Carton, J. A. & Giese, B. S. A reanalysis of ocean climate using Simple Ocean Data Assimilation (SODA). *Mon. Weath. Rev.* **136,** 2999–3017 (2008).
30. Uppala, S. M. *et al.* The ERA-40 re-analysis. *Q. J. R. Meteorol. Soc.* **131,** 2961–3012 (2005).

Author contributions

S.T.K. and W.C. designed the study. S.T.K. performed the data analysis. S.T.K. and W.C. wrote the initial manuscript. All authors discussed the results and contributed to improvement of the manuscript.

Competing financial interests

The authors declare no competing financial interests.